

## REVIEW

# The Agfa Mayneord lecture: MRI of short and ultrashort $T_2$ and $T_2^*$ components of tissues, fluids and materials using clinical systems

G M BYDDER, FRCR

Department of Radiology, University of California San Diego, San Diego, CA, USA

**ABSTRACT.** A variety of techniques are now available to directly or indirectly detect signal from tissues, fluids and materials that have short, ultrashort or supershort  $T_2$  or  $T_2^*$  components. There are also methods of developing image contrast between tissues and fluids in the short  $T_2$  or  $T_2^*$  range that can provide visualisation of anatomy, which has not been previously seen with MRI. Magnetisation transfer methods can now be applied to previously invisible tissues, providing indirect access to supershort  $T_2$  components. Particular methods have been developed to target susceptibility effects and quantify them after correcting for anatomical distortion. Specific methods have also been developed to image the effects of magnetic iron oxide particles with positive contrast. Major advances have been made in techniques designed to correct for loss of signal and gross image distortion near metal. These methods are likely to substantially increase the range of application for MRI.

Received 7 April 2011  
Revised 29 April 2011  
Accepted 30 June 2011

DOI: 10.1259/bjr/74368403

© 2011 The British Institute of  
Radiology

It is a pleasure to thank the president and members of the council of the British Institute of Radiology for the opportunity to honour the memory of Professor Mayneord, who had a pivotal role in founding medical physics in the UK [1, 2]. He was prescient in suggesting in 1945, a time when the use of magnetism in medicine was in disrepute, that the study of magnetic susceptibility could yield both useful and interesting information. This was published in the immediate aftermath of World War II in an issue of the *British Medical Bulletin* celebrating the 50th anniversary of Roentgen's discovery of X-rays [3]. It was also a year before the discovery of nuclear magnetic resonance (NMR), 28 years before the discovery of MRI, and over 40 years before the general use of susceptibility-weighted imaging (SWI) [4, 5] and the observation of the variation in bulk magnetic susceptibility of tendons, ligaments and menisci with orientation to the static magnetic field [6, 7].

It is also a pleasure to acknowledge the critical role of Gordon Higson of the Department of Health in helping to fund the early development of X-ray CT by Sir Godfrey Hounsfield and others at EMI and in supporting the early development of MRI partly from royalties derived from CT [8]. This was a major contribution to the work done by MR groups based in the UK in the late 1970s and led to clinical imaging in 1980–1 [9–14]. A particular regret is the death of Brian Worthington, a close collaborator with both Bill Moore and Sir Peter Mansfield, and author of the first MRI study on a series of patients [13]. Worthington wrote

extensively on neuroradiology, obstetrics and gynaecology, as well as image perception.

During the first year of clinical MRI, only steady-state free precession (SSFP), mobile proton density ( $\rho_m$ ) and  $T_1$  weighted clinical images were available. Clinical heavily  $T_2$  weighted spin-echo (SE) images arrived suddenly in February 1982 and transformed the practice of MRI [15–17]. These images showed abnormalities with high signal and contrast, and they rapidly became the mainstay of clinical diagnosis in the brain. Even with the subsequent development of new types of sequences, such as fast spin echo [18], clinical diffusion weighted imaging [19] and fluid attenuated inversion recovery [20], detection of signal from longer mean  $T_2$  relaxation components still remains the dominant form of MRI for diagnosis of parenchymal disease in the brain and much of the rest of the body.

However, even in 1981, low- or zero-level signals were recognised in cortical bone by Smith [21] and Edelstein et al [22]. The appearance was attributed to short mean  $T_2$  components in this tissue leading to undetectable signal levels at the time of data acquisition. The lack of signal from normal tissue was useful in providing a dark background against which abnormalities in cortical bone, with mean  $T_2$ s sufficiently increased to provide detectable signal, could be recognised; however, the absence of signal meant that there was no possibility of measuring normal values of  $\rho_m$ ,  $T_1$  or  $T_2$ , nor of studying normal perfusion. In addition, there was no opportunity for active contrast manipulation, little or no distinction between adjacent short  $T_2$  tissues and no normal contrast enhancement or effects from molecular imaging agents. As a result, the study of cortical bone and other MR "invisible"

Address correspondence to: Dr Graeme Bydder, Department of Radiology, University of California San Diego, 200 West Arbor Drive, San Diego, CA 92103-8226, USA. E-mail: gbydder@ucsd.edu

short  $T_2$  tissues, such as tendons, ligaments and menisci, has been more limited than that of other tissues, such as brain, liver and muscle, where MR signals are readily detectable with clinical systems.

In spite of these difficulties, there has been a proliferation of new approaches to imaging short  $T_2$  tissue components, including options for developing tissue contrast in the short  $T_2$  and  $T_2^*$  range, as well as methods of imaging in the presence of metal. This has included solutions and partial solutions to technical problems, some of which have appeared intractable for 20 years or more.

The theme of this paper is clinical MRI of "dark matter" (*i.e.* tissues, fluids and materials that show little or no signal with conventional imaging techniques). It includes direct and indirect imaging as well as spectroscopy. As an initial step, some general principles underlying this type of imaging are reviewed.

## General principles

The protons in rigid crystals or solids typically have very short  $T_2$ s due to fixed field effects; however, in solution, motion of molecules leads to averaging of spin interactions over time and much longer  $T_2$ s. This gives rise to the concept of  $\rho_m$ , representing more mobile tissue components with  $T_2$ s that are long compared with those of immobile components. The term "visible" can also be applied to the longer  $T_2$  components since they produce detectable signal, and "invisible" can be applied to short  $T_2$  components, which do not result in detectable signal.

It is important to distinguish between the  $T_2$  of the tissue or fluid that reflects effects such as dipolar-dipolar interactions and chemical exchange, and the observed  $T_2$  ( $T_2^*$ ) of tissues or fluids that also reflects local susceptibility effects, chemical shift and J-coupling, as well as flow, magic angle and other effects. The dominant effect among these is often from susceptibility; this results in a shortening of  $T_2^*$  relative to  $T_2$  due to inhomogeneous magnetic fields within voxels and intravoxel dephasing.

It is often useful to consider relaxivity,  $R_2$  or  $R_2^*$ , which is the reciprocal of  $T_2$  or  $T_2^*$ , *i.e.*  $\frac{1}{T_2}$  or  $\frac{1}{T_2^*}$ , rather than the transverse relaxation times. This is because relaxivities are additive so that, for example, within a voxel

$$\frac{1}{T_2^*} = \frac{1}{T_2} + \gamma\Delta B, \text{ or } R_2^* = R_2 + \gamma\Delta B$$

Thus, the observed relaxivity is the sum of the tissue relaxivity and  $\gamma$  times the inhomogeneity in B (*i.e.*  $\Delta B$ ) within the voxel. Other relaxivities (owing to chemical shift, contrast agents, etc.) can be added in the same way.

When there is a majority of short  $T_2/T_2^*$  components in a tissue, fluid or material, it typically appears low-signal or dark with clinical imaging techniques. A minority of short  $T_2/T_2^*$  components is common in many tissues. In this situation, signal is usually apparent from longer  $T_2/T_2^*$  components, but little or no contribution to the signal comes from the short  $T_2/T_2^*$  components. All tissues have some short  $T_2/T_2^*$  components from protons in large molecules, including those in membranes.

The focus in this paper is on tissue and fluids, but materials may also have short  $T_2/T_2^*$ s and/or low or

zero mobile proton densities. This includes relaxation agents (such as gadolinium chelates) and susceptibility agents (such as magnetic iron oxide particles, MIOs). These materials may produce very large susceptibility differences in tissues and fluids, and can result in very short  $T_2^*$ s. Many materials, including most plastics, also have short  $T_2$ s. Other materials, such as contrast agents and metals, may have no significant  $\rho_m$  but can produce strong effects on surrounding tissues.

There is no precise definition of what constitutes a short echo time (TE) and what is an ultrashort TE (UTE), and there is argument about how TE should be measured for tissues with short  $T_2$ s [23–25]. For simplicity, a short TE is taken to be less than 10 ms, and an ultrashort one less than 1 ms. It is also possible to define short  $T_2/T_2^*$ s as less than 10 ms, ultrashort as less than 1 ms and super-short as less than 0.1 ms. This reflects the fact that, with older MR systems and conventional SE sequences, tissues with  $T_2$ s or  $T_2^*$ s less than 10 ms produced little or no signal and were "invisible". With more recent systems and gradient echo sequences, the cut-off is closer to 1 ms. Ultrashort pulse sequences can often directly detect signal in the 1–0.1 ms range, but indirect methods are usually required to image supershort  $T_2$  (<0.1 ms) tissues.

MR signals are usually spatially encoded using frequency and phase effects produced by linear applied gradient fields. Susceptibility effects also include changes in the local field, and these may result in errors in locating the position of the signal. In fact, the local susceptibility differences may be greater than those of the encoding gradient magnetic field and result in image distortion. This means that, in addition to shortening of  $T_2$  owing to susceptibility effects, resulting in low signal, image distortion may be present with both loss of signal and local "pile up" (*i.e.* increase in signal where signals from different regions are incorrectly superimposed on one another). In general terms, phase encoding tolerates gross field distortion much better than frequency encoding both for slice selection and spatial localization.

Quantitation of tissue or fluid  $T_2^*$ s is made difficult by the addition of other effects; this results in measured values ( $T_2^*$ s) that include effects from local susceptibility and other effects. Measurements may also be confounded by distortion of the spatial encoding process by susceptibility effects. It may also be difficult to assign susceptibility effects to a particular tissue and to distinguish them from inhomogeneity in  $B_0$ . There are also difficulties in accurate measurement of both  $T_2/T_2^*$  values and the relative proportions of two or more different components with the signal-to-noise levels attainable in reasonable times on clinical systems.

Imaging may be regarded as direct when it detects signal from the tissues, fluid or materials of interest, and indirect when the signals are detected from other species that are affected by the short  $T_2/T_2^*$  tissues, fluids or materials of interest. For short  $T_2/T_2^*$  tissues, the most common way of imaging directly is to use a short TE or UTE to detect short  $T_2/T_2^*$  signals before they have decayed to zero or the noise floor. It is also possible to place highly ordered collagen-rich tissues at the magic angle to prolong their  $T_2/T_2^*$ s to make the signal detectable. In other situations it is possible to increase the TE so protons in fat and water, which are out of phase, can become in phase, and the combined signal can then become detectable. Likewise,

spin echo sequences can be used to increase  $T_2^*$  by reversing the effects of local field inhomogeneities.

Indirect forms of imaging short  $T_2/T_2^*$  components include visualisation of the extent of invisible short  $T_2$  tissues when they are surrounded by a longer  $T_2$  tissue with detectable signal. Another indirect method is to observe the effect of short  $T_2$  tissue's susceptibility or relaxation on the surrounding or adjacent longer  $T_2$  tissues. An example of this is to assess trabecular bone by the effect this tissue has on adjacent longer  $T_2^*$  of red or yellow bone marrow. Relaxation agents typically work in this way, with no signal directly detectable from them, but the effects detectable through relaxation or susceptibility effects produced on the protons in associated water or other tissues. A third indirect method is magnetisation transfer (MT), which typically magnetically saturates invisible short  $T_2$  components and results in a change in the magnetisation transferred to the longer  $T_2$  components. This usually results in a shortening of  $T_1$  and a reduction in detectable signal in the detected longer  $T_2$  component.

At present, several different approaches are being used to image short and ultrashort  $T_2$  and  $T_2^*$  tissues, fluids and materials. These may involve both direct and indirect approaches, as well as situations where the primary objective is detection or correction of image distortion owing to susceptibility effects rather than detection of short  $T_2/T_2^*$  signal, although undetectable signals may become detectable as a consequence of this correction.

- The first approach is direct and regards the problem as essentially one of imaging short  $T_2$  components. This can be addressed by using a short TE/UTE and/or a method of increasing  $T_2/T_2^*$  so that signal can be detected from the tissue or fluid. This includes a variety of techniques. This approach is frequently associated with methods of reducing or suppressing the signal from longer  $T_2$  components to isolate the short  $T_2$  components and improve conspicuity or assist with quantitation.
- The second approach is MT that is indirect. This may be extended to invisible tissues by using short TE approaches. The definition of free and bound pools then changes, and there may be increased problems in isolating MT effects because of direct saturation of the newly visible pool.
- The third approach has been termed SWI, where magnitude and/or phase data from a gradient echo sequence are typically used to recognise loss of signal from the tissue itself and/or surrounding tissues if the  $T_2^*$  levels of the tissue are too short to be detectable with the TE in use. This technique can be direct, indirect or both. The TE necessary to produce useful contrast between normal and abnormal tissues in an organ may result in loss of signal in other areas of the image where greater susceptibility differences are present. The basic approach is qualitative and may involve empirical combinations of magnitude and phase data. The technique has limitations in situations where the signal becomes undetectable so that it is not possible to calculate magnitude or phase data, and in situations where the image becomes distorted because of problems in slice selection and/or frequency encoding. A development from this is quantitative susceptibility

imaging (QSI) or susceptibility SWI mapping (SWIM), where approaches are used to assess and correct for the effect of static field perturbations on spatial encoding of the signal and, therefore, to try to avoid compromising signal values. This typically requires the solution to a complex inverse problem, but it is now an area of considerable interest.

- The fourth is positive contrast or white matter imaging, which assesses the effect of MIOPs. These particles typically reduce the signal from tissues as a result of a decrease in  $T_2$  and susceptibility effects. This tends to produce a loss of signal in the area of the image that is of most interest. This can be a particular problem when it occurs in tissues with pre-existing very low signals, so that the reduction is undetectable; however, it is also a problem in other areas where the loss of signal may lead to loss of anatomical detail and poor localisation of the site of contrast agent accumulation. One approach to this problem is to correct the field distortion induced by the MIOPs and allow signal to be detected where these particles accumulate. Different techniques have been used, but the observed result may still reflect both contrast accumulation and field distortions produced by the agent.
- The fifth group of techniques is targeted at imaging in the presence of metal. Metals may show very large susceptibility differences from those of tissues and can produce very large susceptibility effects, with loss of signal due to  $T_2^*$  shortening and gross image distortion. The primary objective in this situation is to deal with the image distortion and restore image integrity to a sufficient degree to make the images clinically useful. In the process, short  $T_2^*$  tissues and fluids may become detectable.

There is an overlap between these approaches, and they may be combined. In some situations, it may be appropriate to ignore the effects of susceptibility differences in producing image distortion and regard the problem as one of detecting short  $T_2$  signals, whereas in others, image distortion due to susceptibility is the primary problem that needs to be addressed.

## Tissue, fluid and material properties

The tissues of the human body can be divided into those that are "visible" in the sense that they provide detectable signal with clinical MR systems and those that are "invisible" because their mean  $T_2$ s or  $T_2^*$ s are too short to provide a detectable signal. All tissues have multicomponent  $T_2$ s. This means that they contain a mixture of short and long  $T_2$  components. The invisible tissues have a majority of short  $T_2$  components and a minority of long  $T_2$  components. The latter components typically do not provide enough signal to be detectable in relation to image noise levels. The "visible" tissues of the body (such as brain, liver and muscle) have a majority of long  $T_2$  components that produce signal with conventional techniques. They also have a minority of short  $T_2$  components, which do not contribute significantly to the detectable signal.

Within the invisible group of tissues (mean  $T_2 < 10$  ms) it is possible to differentiate a first group (including

tendons, ligaments and menisci) with short mean  $T_2$ s of approximately 1–10 ms and a second group (including cortical bone and dentine) with ultrashort mean  $T_2$ s of 0.1–1 ms. There is also a third group (including dental enamel, protons in membranes and molecules, as well as crystalline bone) with supershort mean  $T_2$ s of less than 0.1 ms. Materials can also be classified in a similar way.

An important factor in this context is the magic angle effect [26, 27], because it can greatly increase the  $T_2$  of short  $T_2$  tissues, such as tendons, ligaments and menisci. When the orientation of tissues that contain highly ordered collagen is changed, their  $T_2$  varies from a minimum at  $\theta = 0^\circ$ , where dipolar interactions are greatest, to a maximum at  $3 \cos^2 \theta - 1 \approx 0$  and  $\theta = 55^\circ$ , where  $\theta$  is the orientation of the fibres to  $B_0$ . The increase can be large, for example from 0.6 ms to 21 ms [26] or from 7 to 23 ms [27] in the Achilles tendon.

A recently described phenomenon is directional susceptibility in tendons, whereby their bulk magnetic susceptibility varies with orientation to  $B_0$ , with signals at the water end of the proton spectrum when fibres are parallel to  $B_0$  and at the fat end of the spectrum (lower frequency) when fibres are perpendicular to  $B_0$  [6]. The difference is relatively large (of the order of three parts per million).

The  $\rho_m$  of tissues also varies markedly; bone has a  $\rho_m$  of 15–20%, and semisolid tissues (such as tendons and ligaments) have values of 60–70%.  $\rho_m$  is generally a more important factor in generating contrast with short  $T_2$  tissues than it is with longer  $T_2$  tissues. The low  $\rho_m$  for bone places a limit on the maximum signal that can be obtained from it. Both the low  $\rho_m$  and the short  $T_2^*$  of cortical bone contribute to its low signal intensity.

The mean  $T_1$ s of some tissues with a majority of short  $T_2$  components is short, with cortical bone having a particularly short  $T_1$ ; in fact, less than that of fat [28]. The relative differences in mean  $T_2$  or  $T_2^*$  between normal and abnormal tissues are often much greater than those in mean  $T_1$ .

Relative to air, soft tissues generally show a susceptibility difference of approximately –9 ppm, and bone and calcified tissue approximately –11 ppm. By comparison, the principal peak of fat resonates at approximately –12 ppm. Paramagnetic materials show small positive frequency shifts and superparamagnetic materials show greater positive shifts. Metals (for example titanium), metal alloys and some types of stainless steel may show very large positive shifts of 10 s to 1000 s of parts per million. The changes in field may be considerably greater than machine gradient fields used to encode MR signals, and therefore may cause image distortion.

In disease, increases in  $T_2$  are frequently seen, but decreases in  $T_2$  may be seen with increased iron content and in other disease processes. Loss of magic angle effect may be seen in degeneration and fibrosis.

### Acquisition methods for short $T_2/T_2^*$ components

Some of the techniques now being used to directly detect signal from tissues on clinical systems have been used in material science and tissue studies using small-bore high-field spectrometers for many years. The methods

are now in use on clinical systems that are usually lower performance in terms of  $B_0$ , gradient strength, slew rate and peak  $B_1$  field (Table 1). The prototype sequence for imaging short  $T_2$  tissues is single-point imaging (SPI), where a single point in  $k$ -space is acquired with a UTE. This is typically used with three-dimensional (3D) phase encoding, which tolerates field distortions well, but unfortunately makes the technique time-consuming even with optimised  $k$ -space sampling [29].

It is possible to acquire several points at a time, which makes the sequences more time-efficient, but results in longer TEs for the additional points [30]. There are also free induction decay (FID)-based techniques, where a radial line of  $k$ -space is acquired from the centre out [31]. This can be coupled with long  $T_2$  water and fat suppression to selectively image short  $T_2$  components as water- and fat-suppressed proton projection imaging (WASPI) [32]. Other trajectories in  $k$ -space are possible, including a stack of spirals (SOS) [33] and echo planar imaging (EPI).

A particularly innovative method of imaging short  $T_2$  components is to divide the excitation pulse into sub-pulses and acquire data after each of these pulses. This is known as sweep imaging with Fourier transformation (SWIFT) or simultaneous excitation and acquisition (SEA). The acquired data need to be deconvolved with the excitation pulse, but the end result is a much more time-efficient acquisition than with typical 3D acquisitions [34–37]. Other techniques that have only been used in the pre-clinical phase include methods in which radiofrequency (rf) absorption is assessed rather than signal detection [38]. The methods borrow from continuous wave spectroscopy and electron spin resonance, where electronic  $T_2$ s are extremely short and may be of the order of a microsecond.

### Magnetisation preparation signal suppression techniques and pulse sequences

Traditional contrast mechanisms exploiting differences in  $\rho_m$ , chemical shift and other tissue properties can be used in ways that are already well known from conventional imaging.

There are also numerous old contrast mechanisms operating in new ways, as well as new contrast mechanisms that are of interest in imaging short/ultrashort  $T_2/T_2^*$  components in tissue. They are typically used in conjunction with the acquisition techniques mentioned in the previous section. These provide a wide range of possible ways of effecting magnetisation. For example,  $90^\circ$ ,  $180^\circ$ , fat saturation and magnetisation transfer pulses can all be used to suppress unwanted long  $T_2$  signals and to produce  $T_2$  contrast in the short  $T_2$  range. There are some fairly new potential mechanisms (as far as clinical imaging is concerned) that involve reductions in dipolar coupling [39, 40] and double quantum filters [41]. These techniques are usually used in conjunction with one of the acquisition methods previously described.

### Magnetisation transfer

When used for short  $T_2/T_2^*$  tissues, this differs from conventional clinical approaches because short/UTE

**Table 1.** Short and ultrashort echo time (TE) imaging techniques

Technique	Radiofrequency pulses and gradient	$k$ -space trajectory
Single point [29]	Non-selective hard pulse with gradient applied	3D point-by-point
Multipoint [30]	Hard pulse with gradient applied	3D partial lines Several points
UTE [31, 159–161]	2D two half pulses	Radial from centre out
BLAST [162]	3D hard pulse	FID acquisition
PETRA [163]	No gradient applied during radiofrequency	
ZTE [164]		
BLAST		
PETRA		
ZTE		
WASPI [32]	3D hard pulse with gradient on. Preparation pulses with water and fat signal suppression	Radial from centre out, FID acquisition
Gradient echo	2D, 3D	Radial rephasing gradients
Cones [165]	3D	Spiral, from centre out, FID data collection
Spiral [166]		
Stack of spirals [33]		
Echo planar imaging [167]		
Twisted radial projection [168]		
bSSFP [116, 169]		
bUTE [170]		
VIPR-ATR [171]		
bUTE		
VIPR-ATR		
SWIFT, SEA [34–37]	3D radiofrequency sub-pulses	Radial, centre out

3D, three-dimensional; 2D, two-dimensional; UTE, ultrashort TE; BLAST, back projection low angle shot; PETRA, pointwise encoding time reduction with radial acquisition; ZTE, zero TE; WASPI, water- and fat-suppressed proton projection imaging; FID, free induction decay; bSSFP, balanced steady-state free precession; bUTE, balanced UTE; VIPR-ATR, vastly undersampled isotropic projection reconstruction-alternating length repetition times; SWIFT, sweep imaging with Fourier transformation; SEA, simultaneous excitation and acquisition.

acquisitions make it possible to study MT in tendons, ligaments, menisci and cortical bone [42], and tendon [43]. The definition of the bound (short  $T_2$ ) and free (long  $T_2$ ) pools may change because previously undetected signals are included in the free (detectable) pool. Direct saturation is a greater problem. There may be a greater degree of magnetisation exchange present in short mean  $T_2$  tissues. The technique provides indirect access to supershort  $T_2$  relaxation components in tissues with  $T_{2S}$  of approximately 5–15  $\mu$ s, which are not directly accessible with most UTE techniques.

### Susceptibility-weighted imaging

SWI has been in use for a considerable amount of time. It usually exploits reductions in  $T_2^*$  to develop contrast; the imaging may use both magnitude and phase data [44, 45]. The  $T_2^*$  may be so short that it becomes, in effect, an indirect form of imaging using the reduction in signal of adjacent longer  $T_2$  components. The applicability of the technique and related methods can be expanded by using forms of data collection with short TEs or UTEs that can detect signal from very short  $T_2^*$  components [46, 47]. Quantitative methods of imaging susceptibility changes need to account for errors in spatial encoding, which may require solutions to complex inverse problems [48, 49]. To date, the techniques have mainly been applied to brain imaging. Phase and frequency changes can be detected in ordered fibrous structures even with UTE sequences [47].

### Positive contrast and white marker imaging

These forms of imaging have been used to describe particular situations with MIOPs that may not only reduce  $T_2$  and  $T_2^*$ , but produce local field distortions. A variety of different methods are available. It is possible to selectively excite only off-resonance spins. It is also possible to apply an additional gradient so that only the magnetisation of spins in regions affected by MIOPs is refocused. The inhomogeneities from the particles induce echo shifts, and these can be used to calculate and correct for the field distortion. The images reflect both tissue MIOP concentration and deviations of the local magnetic field produced by the particles [50–54]. Techniques using SWIFT [55] and UTE [56–58] have also been successful for imaging MIOPs.

### Imaging in the presence of metal

When forms of metal are implanted in the body, an extreme situation may arise in which there is very marked  $T_2^*$  shortening, but the image distortion is so great that images of regions adjacent to the metal cannot be interpreted. This has been a longstanding problem. A variety of solutions have been proposed in the past, but these have had relatively little clinical impact. The recent development of multi-acquisition variable-resonance image combination (MAVRIC) [59] and slice encoding for metal artefact correction (SEMAC) [60] has resulted in a remarkable degree of restoration of images that are grossly degraded by metallic artefact when imaged using

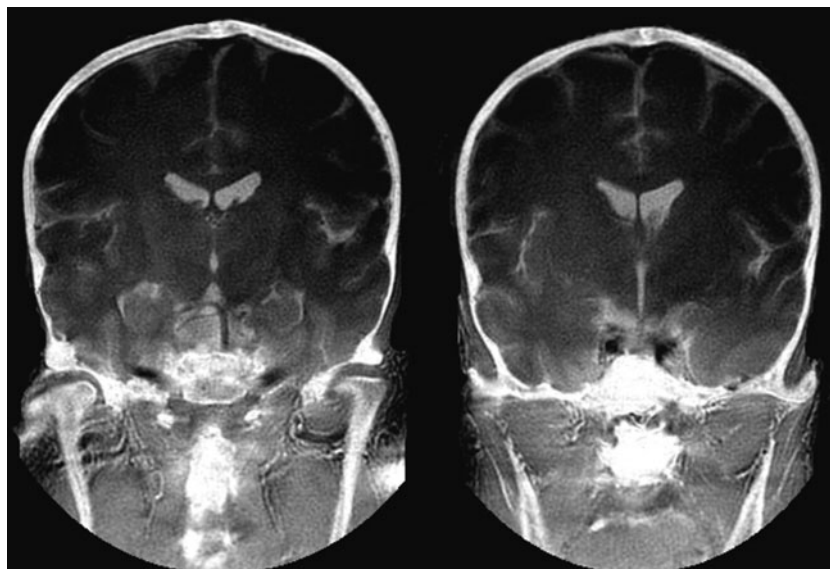


**Figure 1.** Ultrashort echo time subtraction MRI of the skull. The inner and outer tables are seen in a manner similar to X-ray computed tomography displayed with bone windows.

conventional approaches [61]. The use of MAVRIC irradiation and detection of signal at the same off-resonance frequency can image signals for which the resonant frequency has been shifted by metal. The results from different off-resonance frequencies are then combined. SEMAC uses phase encoding during slice selection to relocate signals that are improperly located by the slice selection process. View angle tilting (VAT) [62] is then used with this technique to correct for errors with in-plane spatial encoding. Faster versions [63, 64] and a MAVRIC–SEMAC hybrid [65] have also been implemented; the term multispectral imaging (MSI) has been applied to these approaches. UTE alone shows an improvement over conventional techniques [66], but this technique may be more effective in combination with MAVRIC [67]. It may also be used in the form of radial sampling with off-resonance recognition (RASOR) [68]. There is continued technical progress in mapping gradient and  $B_1$  distortion [69, 70].

### Imaging of boundaries involving short $T_2/T_2^*$ tissues

Structures of interest in the short  $T_2$  range include thin layers (such as those in entheses, periosteum and the deep layers of articular cartilage where there are short  $T_2$  tissues), susceptibility effects between the soft (or semisolid) tissues and bone, as well as partial volume effects between these tissues that are present over curved surfaces. In this situation, high-resolution 3D isotropic UTE imaging often has a distinct advantage since it can detect short  $T_2/T_2^*$  signals as well as reduce the impact of susceptibility differences and partial volume effects. Imaging of ordered fibrous structures, such as tendons and ligaments, include some of the above issues, but loss of contrast of the fibre structure or “blurred” appearance may arise from obliquity of the fibres relative to the imaging slice. This effect may simulate changes due to disease. There are also distinctive artefacts at boundaries from chemical shift effects, including those associated with radial acquisitions.

### Clinical proton applications

There are now two-dimensional (2D) and 3D UTE sequences available with imaging times of 5–6 min and clinically acceptable spatial resolutions [33, 71]. In general, the difficulty of acquiring short/ultrashort  $T_2/T_2^*$  signals means that invisible tissues are imaged at lower spatial resolution, but with signal levels and contrast that are not attainable with conventional techniques. There is a balance necessary to obtain qualitative and/or quantitative information that is novel with spatial resolutions that are sufficient to show anatomical features with acceptable clarity.

### Cortical bone

Cortical bone can be demonstrated with high signal [28]. Its  $T_2$  is about 0.4 ms and  $T_1$  250–350 ms at 1.5 T, which is shorter than typical values for fat. Its mobile proton density is about 15–20%. Detectable signal can be used for both quantitative and qualitative studies [72–77] (Figures 1 and 2), as well as for comparison with spectroscopic studies [78]. UTE measurements of bone may be of value for attenuation corrections in PET/MRI [79, 80].

### Tendons, ligaments and entheses

With conventional sequences, the signal from tendons, ligaments and entheses is very low or zero. Entheses are the attachment sites of tendons, ligaments and capsules to bone. They typically contain calcified and uncalcified fibrocartilage, which both have short  $T_2$ s. These tissues have a major role in dispersing mechanical stress at the junction between flexible tendons or ligaments and rigid bone.

Tendons and ligaments contain endotenon and endoligament, which have longer  $T_2$ s than the fibrous components (although they are still in the short  $T_2$  range) and less magic angle effect. Uncalcified fibrocartilage has a longer  $T_2$  than the tensile components of

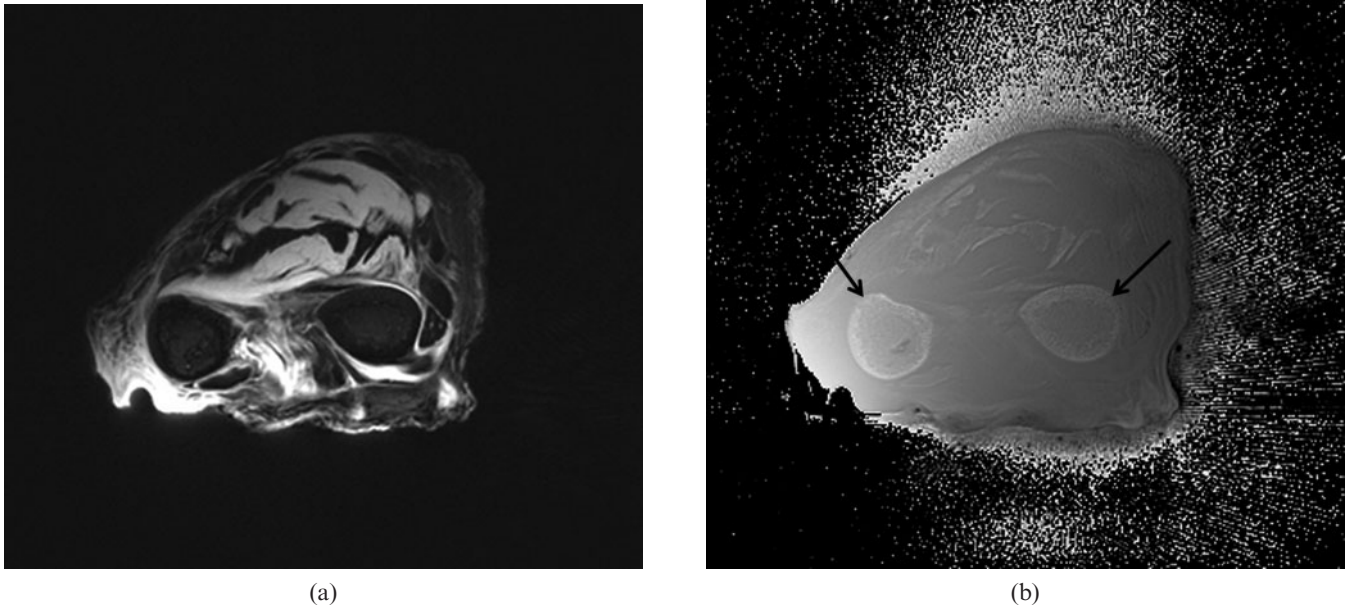


**Figure 2.** (a) Transverse magnitude and (b) phase images of the forearm with a ultrasound echo time ( $TE$ ;  $-12 \mu s$ ) sequence. Differences in phase are seen between the cortical bone of the radius and ulnar (arrows) and the surrounding soft tissues, as well as between muscle and tendon in (b).

tendons, as well as an increase in  $T_2$  due to the magic angle effect, although this may be present over a wider range of angles and reflects the more dispersed arrangement of the fibres within it.

Tendons and ligaments can be seen readily with UTE sequences and entheses have been studied in detail [81–83]. Off-resonance fat suppression pulses reduce the signal from short  $T_2$  fibres (which have a broad linewidth) more than endotenon or enthesis fibrocartilage (which have longer  $T_2$ s and narrower linewidths), and this can be an effective contrast mechanism. Inversion pulses may be used to selectively invert and null enthesis fibrocartilage (exploiting its longer  $T_2$ ) and so visualise this tissue with high contrast. It is also possible to visualise oblique and transverse fibres in tendons using a combination of fat-suppressed UTE sequences to reduce short  $T_2$  tissue water components and magic angle imaging to lengthen the  $T_2$  of the fibres at particular angles to  $B_0$  (Figure 3).

Entheses are selectively involved in the seronegative spondyloarthropathies, such as ankylosing spondylitis and psoriatic arthropathy. The differential diagnosis is of a loss or reduction in fascicular pattern, and includes normal sesamoid fibrocartilage, partial volume effects with a loss of fascicular pattern due to partial volume effects, magic angle effects and disease.

### The menisci of the knee

The central region of the adult meniscus has no blood supply (the white zone), while the more peripheral region (the red zone) does have one. Healing of tears in the white zone is often unsatisfactory and the preferred surgical strategy is usually resection of the torn tissue. Suture and repair is more successful in the red zone. Distinction between the two zones has not previously been possible with MRI using conventional sequences, in spite of repeated

attempts [84]. Using UTE sequences and gadolinium-based contrast enhancement, the two zones can be distinguished [79] and provide a basis for surgical planning.

Anatomical descriptions of the meniscus include circumferential, radial, lamella, vertical and meshwork fibre groups. With conventional imaging, some radial

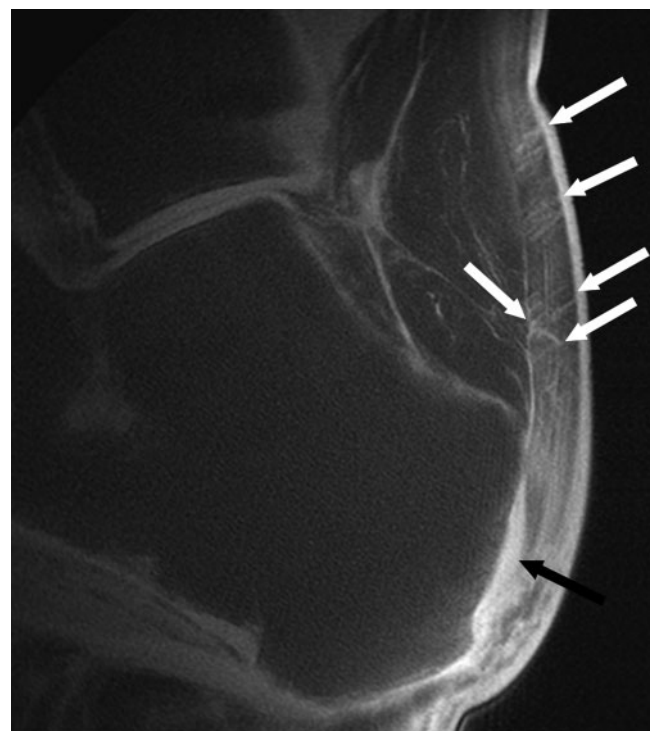


**Figure 3.** Sagittal short echo time image of the Achilles tendon. Oblique fibres at the magic angle are seen within the tendon (white arrows). Fibrocartilage of the tendon enthesis is also seen as a high-signal area (black arrow).

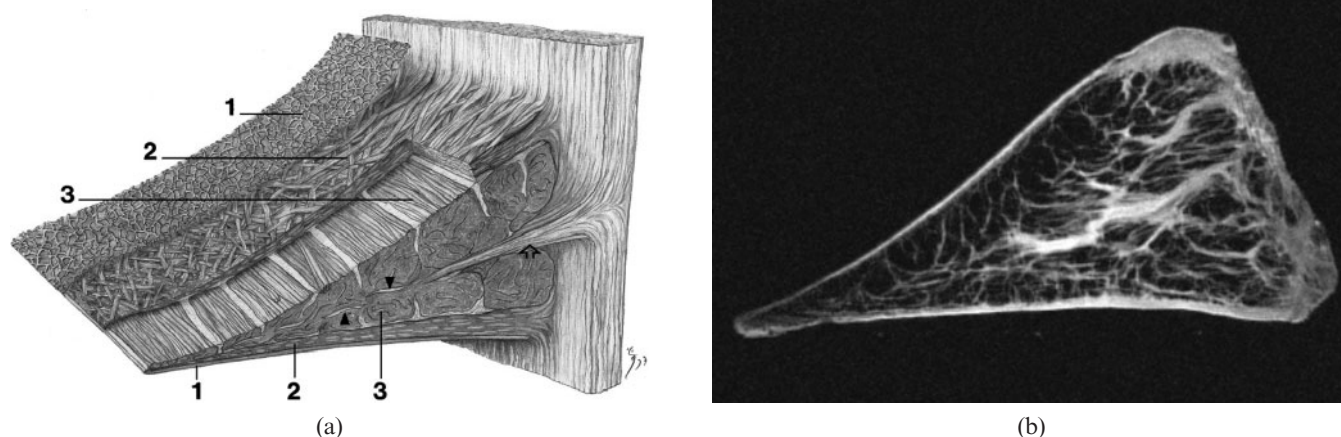


**Figure 4.** (a) Diagram of the fibre structure of the meniscus from Petersen and Tillmann [172] (with permission), and (b) short echo time image of the meniscus. In (a) a very thin (30 nm) layer is shown (1) with the lamella (2) and circumferential fibres (3). In (b) layer (1) is not seen, but the external lamella fibres are seen as high-signal on the surface of the meniscus and extensive radial fibres are seen within the meniscus.

fibres may be distinguishable from the majority of circumferential fibres [84], but with UTE and magic angle imaging, each of these fibre groups can be identified (Figure 4) [85–90]. It is also possible to distinguish the internal structure of the meniscus from that of the root ligaments (Figure 5), and the more central cartilaginous region from the peripheral, more fibrous region of the meniscus.

The fibre structure provides a basis for understanding the biomechanics of the knee and the various patterns of tears in the meniscus. It also helps in distinguishing magic angle effects within fibre groups from degenerative changes. Quantitative studies of  $T_1\rho$  and  $T_2$  may be informative [91–93]. Quantitative studies including repair have also been of value [94].

The temporomandibular joint disc shows some of the characteristics of the meniscus of the knee. Fibre structure can be seen. Lamella, circumferential antero-posterior and superoinferior fibres are identifiable (Figure 6).

### Articular cartilage

Articular cartilage has a range of  $T_2$ s from approximately 1 to 30–40 ms, from deep to superficial. When using conventional imaging, the deep radial and calcified layers, as well as the adjacent subchondral bone, are invisible. In UTE imaging, the signal is detectable from the deeper layers of cartilage, allowing

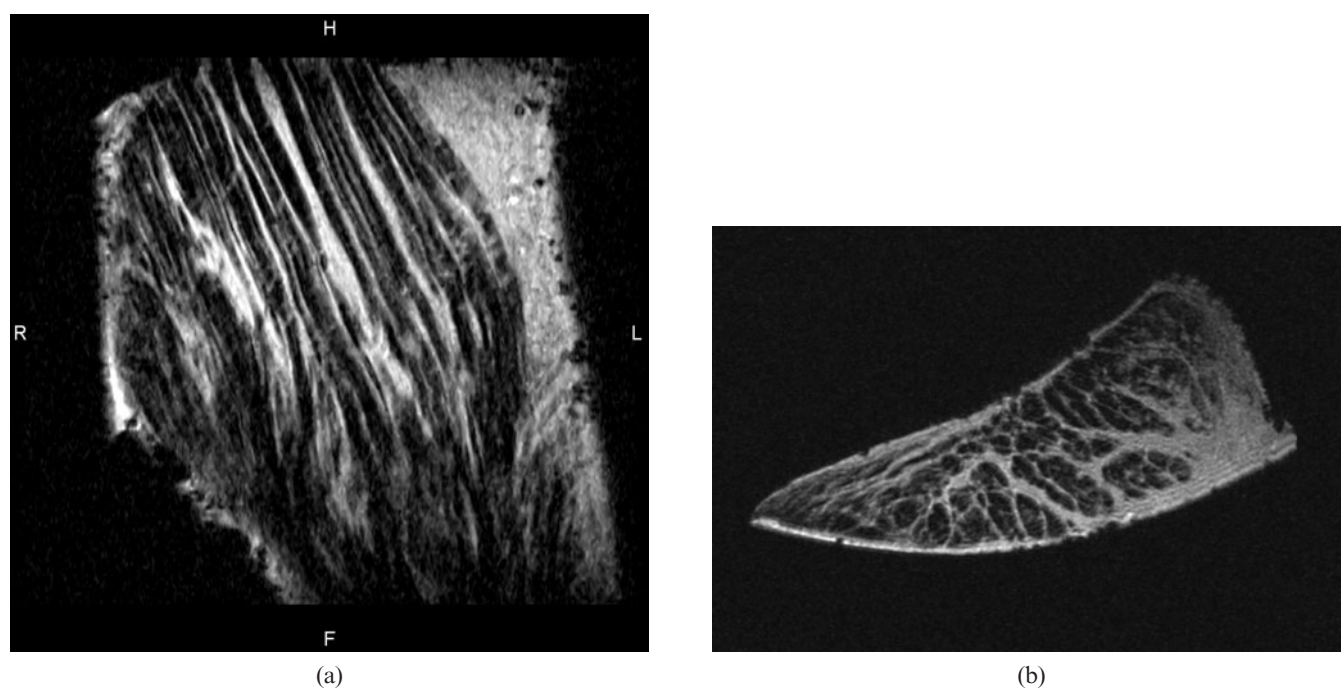


**Figure 5.** (a) Longitudinal and (b) transverse short echo time images of the root ligament of the meniscus. Linear high-signal endoligament and fine transverse fibres are seen in (a). High-signal endoligament extending across the ligament is seen in (b).

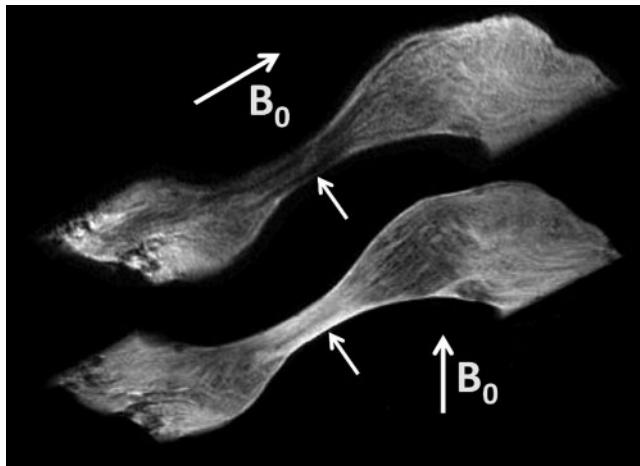


**Figure 6.** Sagittal short echo time image of the temporomandibular disc at different relations to  $B_0$  (arrows). The intermediate zone is low-signal in the upper image with anteroposterior and lamella fibres parallel to  $B_0$ , and high-signal when these fibres are at the magic angle (lower image).

more superficial cartilage and subchondral bone to be distinguished [95–99]. This provides a basis for study of the junction between the cartilage and bone, which may be important in the pathogenesis of osteoarthritis. Complex magic angle effects are seen because of the fibrous architecture of articular cartilage.

In disease, there may be loss of signal from the deep layer and increased extent of the short  $T_2$  associated with deep layers. There is electron microscopic evidence of thinning of the deep layers in osteoarthritis, but preservation in osteomalacia.

## Spine

Imaging of the spine includes many visible tissues, which means attention to date has focused on invisible structures such as entheses, the end plate of the disc [100, 101], and short  $T_2$  components in the intervertebral discs and red bone marrow. Fibrocartilage has also been demonstrated in the functional entheses of the transverse ligament of the atlas and the alar ligament. The dorsal capsules of the facet joints of the lumbar spine are also subject to cartilagenous metaplasia. Evidence of iron deposition can be seen in intervertebral discs in thalassaemia [102]. Sclerotic metastases and cement after vertebroplasty have been identified [103, 104]. The structure of the annulus fibrosus can be demonstrated (Figure 7). The pattern of alternating fibres between lamellae is well demonstrated.

## Central nervous system

There are significant short  $T_2$  components in many tissues of the body with longer mean  $T_2$ s, including brain, spinal cord and peripheral nerve. These components can be specifically detected using UTE and other acquisition methods coupled with techniques that suppress long  $T_2$

signals [105–107]. It is possible to specifically image short  $T_2$  components in myelin and use these to map white matter and identify disease [108–113].

## Lung and heart

Imaging of the lung was the first application of UTE imaging [31]. More recent studies have identified emphysema, cystic fibrosis and other conditions [114–120].

Fibrosis has been identified in the heart [121].

## Liver

The liver contains a relatively high proportion of short  $T_2$  components. The  $T_2$ s of these may be prolonged in fibrosis [122]. Fibrosis in this situation is often of a relatively open structure and includes free water.

## Pelvis

UTE sequences have found application in studying the effects of cryosurgery in carcinoma of the prostate [123]. Freezing of tissues results in a substantial reduction in  $T_2^*$  [124].

## Atherosclerotic plaque

Short  $T_2$  components and calcification have been identified and characterised in atherosclerotic plaque [125–127].

## Other proton applications

Contrast enhancement with gadolinium chelates may be seen within previously invisible tissues using UTE sequences [128], as well as with MIOPs [50–58]. Dental imaging has successfully identified caries [129–131]. Mummified tissue has also been studied [132].

## Other nuclei

Sodium imaging has a long history, with the principal applications in the brain [133–138], heart [139], kidney [140, 141] and musculoskeletal system [142–144]. Phosphorus imaging has also been performed with UTE sequences [145, 146]. Oxygen-17 studies have been performed in the brain [135, 137], and fluorine studies have begun [147].

## Quantitative approaches

Quantitation may include specific MR properties, particularly  $T_2$  and  $T_2^*$  [148–152], the properties of the remaining signal after long  $T_2$  components are suppressed and the ratio of short  $T_2$  to long  $T_2$  components. There are other features (such as the magic angle effect and dipolar contrast) that can be characterised [153, 154], as well as susceptibility effects (Figure 8).

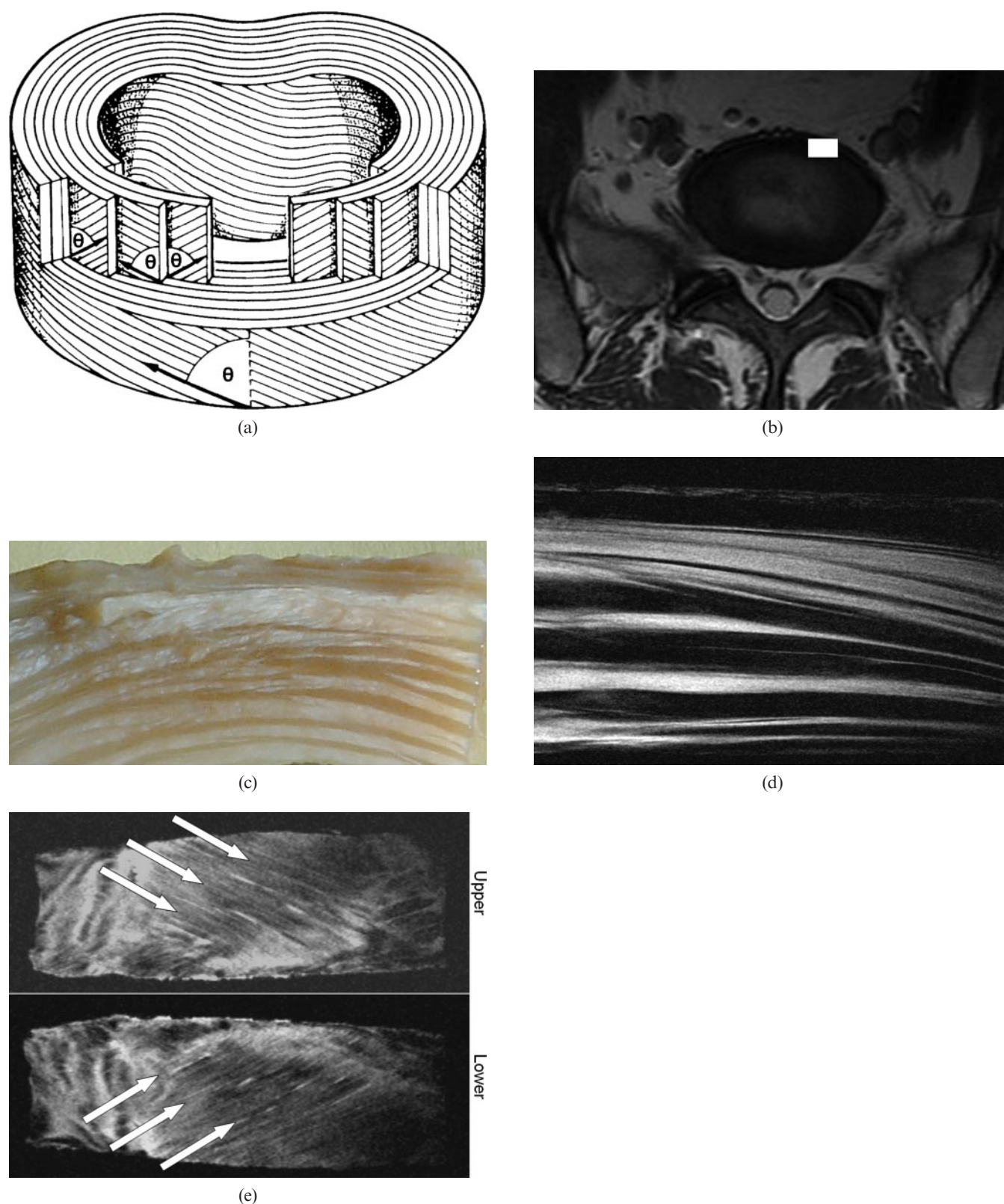


**Figure 7.** (a) Diagram of the annulus of the intervertebral disc from Bogduk [173] (with permission), (b) axial image of the L5/S1 disc, (c) photograph of a segment of an annulus of the disc, (d) the corresponding fibre structure seen with a short echo time (TE) sequence and (e) oblique coronal views of adjacent lamella. The lamella structure of the disc is shown in (a) with alternating layers of fibres at angle  $\theta$  to the plane of the disc. An L5/S1 disc is shown in (b) with the white rectangle showing a section of the annulus as seen in (c). A short TE image (d) shows high signal from some lamellae and extracellular matrix, and low signal from other lamellae, following a generally alternating pattern. (e) Arrows show the fibre directions in alternate lamella at  $\theta=25^\circ$  to the plane of the disc.

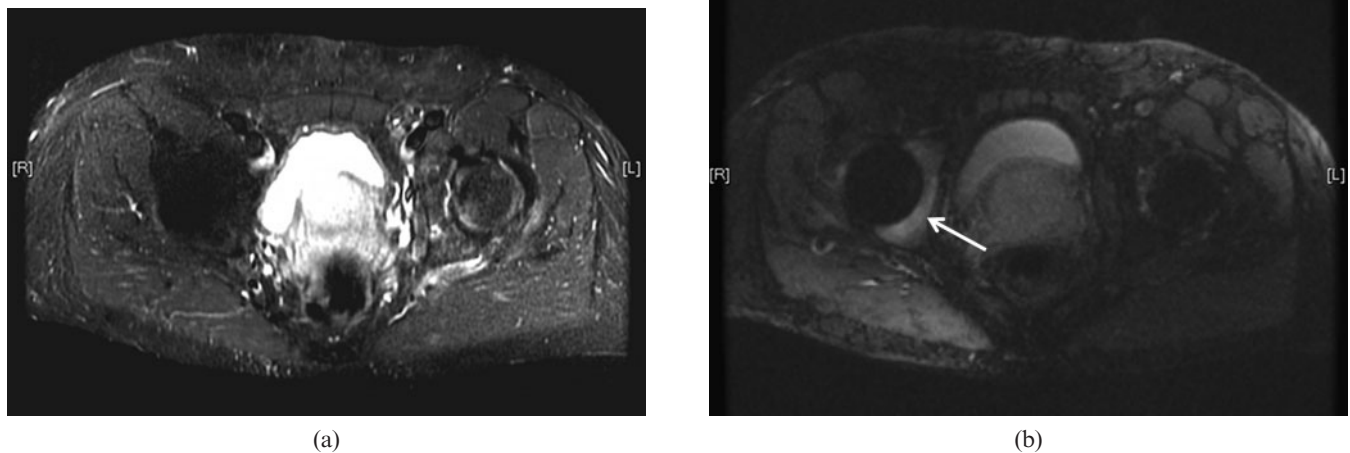


**Figure 8.** (a) Conventional short tau inversion recovery (STIR) image of a prosthesis of the right hip and (b) slice encoding for metal artefact correction STIR image of the same region. The bone marrow of the acetabulum shows an increased signal in (b) (arrow). This area is not seen in (a).

There are issues regarding measuring  $T_2$  and  $T_2^*$  in the correct range, characterising different  $T_2$  components (e.g. long and short), including their relative proportions, and dealing with artefacts from various sources. Quantitation may be confounded by slice selection, problems with eddy currents and by contamination of short  $T_2$  components with long  $T_2$  components that are present in higher concentration.

### Artefacts

Short time-constant eddy currents and gradient timing errors may result in artefacts and errors in measurement that can be corrected [155–158].

### Conclusion

Imaging of short  $T_2$  and  $T_2^*$  components is an expanding area of application for MRI, which has seen a convergence of methods primarily targeted at tissues with short  $T_2$  components, SWI, MIOP imaging and metal artefact control. The methods have borrowed from solid-state imaging, spectroscopy (including continuous wave methods), electron spin resonance and MR microscopy. The much lower technical performance of clinical systems compared with small-bore spectrometers is a major limitation, but innovative methods for overcoming this problem are now being developed.

The tissues of interest have mainly been in the musculoskeletal system, but all tissues of the body have some short  $T_2$  components, and study of these may prove to be of diagnostic importance. Some techniques, such as imaging in the presence of metal (Figure 8), are likely to be immediately useful in the clinical domain, while others will probably require validation and comparative assessment to establish their role. Quantitative approaches may be useful given the large fractional changes in short  $T_2$  and  $T_2^*$  components that may be seen in disease. The techniques used for imaging often require high-gradient performance with control of short-term eddy currents to a level not previously thought necessary in clinical MR

systems. In spite of these and other technical difficulties, application of the study for short  $T_2$  and  $T_2^*$  tissues appears to be an area of MRI that will be of considerable importance in the near future.

### Acknowledgments

The author has received grant support from the National Institutes of Health and General Electric Healthcare.

### References

1. Spiers FW. William Valentine Mayneord. *Biogr Mems Fell R Soc* 1991;37:343–64.
2. Lamerton LF. Obituary Professor W V Mayneord CBE, DSc, FInstP, FRS. *Br J Radiol* 1988;61:1093–4.
3. Mayneord WV. Physics in medicine. *Br Med Bull* 1945;3: 129–32.
4. Young IR, Khenia S, Thomas DG, Davis CH, Gadian DG, Cox IJ, et al. Clinical magnetic susceptibility mapping of the brain. *J Comput Assist Tomogr* 1987;11:2–6.
5. Haacke EM, Reichenbach JR (eds). *Susceptibility weighted imaging in MRI: basic concepts and clinical applications*. Hoboken, NJ: Wiley-Blackwell, 2011.
6. Krasnosselskaia LV, Fullerton GD, Dodd SJ, Cameron IL. Water in tendon: orientational analysis of the free induction decay. *Magn Reson Med* 2005;54:280–88.
7. Du J, Chiang AJ, Chung CB, Statum S, Znamirovski R, Takahashi A, et al. Orientational analysis of the Achilles tendon and enthesis using an ultrashort echo time spectroscopic imaging sequence. *Magn Reson Imag* 2010;28:178–84.
8. Higson GR. Seeing things more clearly. *Br J Radiol* 1987;60:1049–57.
9. Mallard JR. Magnetic resonance imaging—the Aberdeen perspective on developments in the early years. *Phys Med Biol* 2006;51:R45–60.
10. Smith FW, Mallard JR, Hutchison JM, Reid A, Johnson G, Redpath TW, et al. Clinical application of nuclear magnetic resonance. *Lancet* 1981;1:78–9.
11. Mansfield P. Snapshot magnetic resonance imaging (Nobel Lecture). *Angew Chem Int Ed Engl* 2004;43: 5456–64.

12. Hinshaw WS, Andrew ER, Bottomley PA, Holland GN, Moore WS. Display of cross sectional anatomy by nuclear magnetic resonance imaging. *Br J Radiol* 1978;68:173–81.
13. Hawkes RC, Holland GN, Moore WS, Worthington BS. Nuclear magnetic resonance (NMR) tomography of the brain: a preliminary clinical assessment with demonstration of pathology. *J Comput Assist Tomogr* 1980;4:577–86.
14. Young IR, Hall AS, Pallis CA, Legg NJ, Bydder GM, Steiner RE. Nuclear magnetic resonance imaging of the brain in multiple sclerosis. *Lancet* 1981;2:1063–6.
15. Bailes DR, Young IR, Thomas DJ, Straughan K, Bydder GM, Steiner RE. NMR imaging of the brain using spin-echo sequences. *Clin Radiol* 1982;33:395–414.
16. Bydder GM, Steiner RE, Young IR, Hall AS, Thomas DJ, Marshall J, et al. Clinical NMR imaging of the brain: 140 cases. *AJR Am J Roentgenol* 1982;139:215–36.
17. Crooks LE, Mills CM, Davis PL, Brant-Zawadzki M, Hoenninger J, Arakawa M, et al. Visualization of cerebral and vascular abnormalities by NMR imaging. The effects of imaging parameters on contrast. *Radiology* 1982;144:843–52.
18. Hennig J, Nauerth A, Friedburg H. RARE imaging: a fast imaging method for clinical MR. *Magn Reson Med* 1986;3:823–33.
19. Le Bihan D, Breton E, Lallemand D, Grenier P, Cabanis E, Laval-Jeantet M. MR imaging of intravoxel incoherent motions: application to diffusion and perfusion in neurologic disorders. *Radiology* 1986;161:401–7.
20. De Coene B, Hajnal JV, Gatehouse P, Longmore DB, White SJ, Oatridge A, et al. MR of the brain using fluid-attenuated inversion recovery (FLAIR) pulse sequences. *AJNR Am J Neuroradiol* 1992;13:1555–64.
21. Smith FW. Clinical application of NMR tomographic imaging. In: Witcofski RL, Karstaedt N, Partain CL (eds). *NMR imaging*. Winston Salem, NC: Bowman Gray School of Medicine; 1982:125–32.
22. Edelstein WA, Bottomley PA, Hart HR, Leue WM, Schenck JF, Redington RW. NMR imaging at 5.1 MHz: work in progress. In: Witcofski RL, Karstaedt N, Partain CL (eds). *NMR imaging*. Winston Salem, NC: Bowman Gray School of Medicine; 1982:139–45.
23. Robson MD, Gatehouse PD, Young IR, Bydder GM. Ultrashort TE (UTE) imaging of short  $T_2$  relaxation components: how should the  $T_2$  weighting be described? *Proc Intl Soc Mag Reson Med* 2004;11:636.
24. Robson MD, Gatehouse PD. Consequences of  $T_2$  relaxation during half-pulse slice selection for ultrashort TE imaging. *Magn Reson Med* 2010;64:610–5.
25. Springer F, Steidle G, Martirosian P, Claussen CD, Schick F. Effects of in-pulse transverse relaxation in 3D ultrashort echo time sequences: analytical derivation, comparison to numerical simulation and experimental application at 3T. *J Magn Reson* 2010;206:88–96.
26. Fullerton GD, Cameron IL, Ord VA. Orientation of tendons in the magnetic field and its effect on  $T_2$  relaxation times. *Radiology* 1985;155:433–5.
27. Henkelman RM, Stanisz GJ, Kim JK, Bronskill MJ. Anisotropy of NMR properties of tissue. *Magn Reson Med* 1994;32:592–601.
28. Reichert IL, Robson MD, Gatehouse PD, He T, Chappell KE, Holmes J, et al. Magnetic resonance imaging of cortical bone with ultrashort TE pulse sequences. *Magn Reson Imaging* 2005;23:611–18.
29. Chen Q, Halse M, Balcom BJ. Centric scan SPRITE for spin density imaging of short relaxation time porous materials. *Magn Reson Imaging* 2005;23:263–6.
30. Fernandez-Seara MA, Wehrli SL, Wehrli FW. Multipoint mapping for imaging of semi-solid materials. *J Magn Reson* 2003;160:144–50.
31. Bergin CJ, Pauly JM, Macovski A. Lung parenchyma: projection reconstruction MR imaging. *Radiology* 1991;179:771–81.
32. Wu Y, Ackerman JL, Chesler DA, Graham L, Wang Y, Glimcher MJ. Density of organic matrix of native mineralized bone measured by water-and-fat suppressed proton projection MRI. *Magn Reson Med* 2003;50:59–68.
33. Qian Y, Boada FE. Acquisition-weighted stack of spirals for fast high-resolution three-dimensional ultra-short echo time MR imaging. *Magn Reson Med* 2008;60:135–45.
34. Idiyatullin D, Corum C, Park JY, Garwood M. Fast and quiet MRI using a swept radiofrequency. *J Magn Reson* 2006;181:342–49.
35. Idiyatullin D, Corum C, Moeller S, Garwood M. Gapped pulses for frequency-swept MRI. *J Magn Reson* 2008;193:267–73.
36. Blümlich B, Gong Q, Byrne E, Greferath M. NMR with excitation modulated by Frank sequences. *J Magn Reson* 2009;199:18–24.
37. Weiger M, Hennel F, Pruessmann KP. Sweep MRI with algebraic reconstruction. *Magn Reson Med* 2010;64:1685–95.
38. Fagan AJ, Davies GR, Hutchison JM, Glasser FP, Lurie DJ. Development of a 3-D multi-nuclear continuous wave NMR imaging system. *J Magn Reson* 2005;176:140–50.
39. Grenier D, Pascui O, Briguet A. Dipolar contrast for dense tissues imaging. *J Magn Reson* 2000;147:353–6.
40. Regatte RR, Schweitzer ME, Jerschow A, Reddy R. Magic sandwich echo relaxation mapping of anisotropic systems. *Magn Reson Imaging* 2007;25:433–8.
41. Navon G, Eliav U, Demco DE, Blümlich B. Study of order and dynamic processes in tendon by NMR and MRI. *J Magn Reson Imaging* 2007;25:362–80.
42. Springer F, Martirosian P, Machann J, Schwenzee NF, Claussen CD, Schick F. Magnetization transfer contrast imaging in bovine and human cortical bone applying an ultrashort echo time sequence at 3 Tesla. *Magn Reson Med* 2009;61:1040–8.
43. Hodgson RJ, Evans R, Wright P, Grainger AJ, O'Connor PJ, Helliwell P, et al. Quantitative magnetization transfer ultrashort echo time imaging of the Achilles tendon. *Magn Reson Med* 2011;65:1372–6.
44. Haacke EM, Mittal S, Wu Z, Neelavalli J, Cheng YC-N. Susceptibility-weighted imaging: technical aspects and clinical applications, part 1. *AJNR Am J Neuroradiol* 2009;30:19–30.
45. Mittal S, Wu Z, Neelavalli J, Haacke EM. Susceptibility-weighted imaging: technical aspects and clinical applications, part 2. *AJNR Am J Neuroradiol* 2009;30:232–52.
46. Du J, Chiang AJ, Chung CB, Statum S, Znamirski R, Takahashi A, et al. Orientational analysis of the Achilles tendon and enthesis using an ultrashort echo time spectroscopic imaging sequence. *Magn Reson Imaging* 2010;28:178–84.
47. Du J, Carl M, Bydder GM. Ultrashort TE imaging: phase and frequency mapping of susceptibility effects in short  $T_2$  tissues of the musculoskeletal system. In: Reichenbach JR, Haacke EM (eds). *Susceptibility weighted imaging in MRI: basic concepts and clinical applications*. Hoboken, NJ: Wiley-Blackwell; 2011:669–96.
48. Schäfer A, Wharton S, Gowland P, Bowtell R. Using magnetic field simulation to study susceptibility-related phase contrast in gradient echo MRI. *Neuroimage* 2009;48:126–37.
49. de Rochefort L, Liu T, Kressler B, Liu J, Spincemille P, Lebon V, et al. Quantitative susceptibility map reconstruction from MR phase data using bayesian regularization: validation and application to brain imaging. *Magn Reson Med* 2010;63:194–206.

50. Cunningham CH, Arai T, Yang PC, McConnell MV, Pauly JM, Conolly SM. Positive contrast magnetic resonance imaging of cells labeled with magnetic nanoparticles. *Magn Reson Med* 2005;53:999–1005.
51. Suzuki Y, Cunningham CH, Noguchi K, Chen IY, Weissman IL, Yeung AC, et al. In vivo serial evaluation of superparamagnetic iron-oxide labeled stem cells by off-resonance positive contrast. *Magn Reson Med* 2008;60:1269–75.
52. Liu W, Frank JA. Detection and quantification of magnetically labeled cells by cellular MRI. *Eur J Radiol* 2009;70:258–64.
53. Dahnke H, Liu W, Herzka D, Frank JA, Schaeffter T. Susceptibility gradient mapping (SGM): a new post-processing method for positive contrast generation applied to superparamagnetic iron oxide particle (SPIO)-labeled cells. *Magn Reson Med* 2008;60:595–603.
54. Liu W, Dahnke H, Rahmer J, Jordan EK, Frank JA. Ultrashort  $T_2^*$  relaxometry for quantitation of highly concentrated superparamagnetic iron oxide (SPIO) nanoparticle labeled cells. *Magn Reson Med* 2009;61:761–6.
55. Zhou R, Idiyatullin D, Moeller S, Corum C, Zhang H, Qiao H, et al. SWIFT detection of SPIO-labeled stem cells grafted in the myocardium. *Magn Reson Med* 2010;63:1154–61.
56. Crowe LA, Wang Y-X, Gatehouse P, Tessier J, Waterton J, Robert P, et al. Ex vivo MR imaging of atherosclerotic rabbit aorta labeled with USPIO – enhancement of iron loaded regions in UTE imaging. *Proc Intl Soc Mag Reson Med* 2005;13:115.
57. Girard OM, Du J, Agemy L, Sugahara KN, Rotamraju VR, Ruoslahti E, et al. Optimization of iron oxide nanoparticle detection using ultrashort echo time pulse sequences: comparison of  $T_1$ ,  $T_2^*$ , and synergistic  $T_1$ - $T_2^*$  contrast mechanisms. *Magn Reson Med* 2011;65:1649–60.
58. Zhang L, Zhong X, Wang L, Chen H, Wang YA, Yeh J, et al.  $T_1$ -weighted ultrashort echo time method for positive contrast imaging of magnetic nanoparticles and cancer cells bound with the targeted nanoparticles. *J Magn Reson Imaging* 2011;33:s194–202.
59. Koch KM, Lorbiecki JE, Hinks RS, King KF. A multi-spectral three-dimensional acquisition technique for imaging near metal implants. *Magn Reson Med* 2009;61:381–90.
60. Lu W, Pauly KB, Gold GE, Pauly JM, Hargreaves BA. SEMAC: slice encoding for metal artifact correction in MRI. *Magn Reson Med* 2009;62:66–76.
61. Koff MF, Hayter CL, Shah P, Koch KM, Miller TT, Potter HG. Magnetic resonance imaging of arthroplasty: comparison of MAVRIC and conventional fast spin echo techniques. *Proc Intl Soc Mag Reson Med* 2011;19:289.
62. Cho ZH, Kim DJ, Kim YK. Total inhomogeneity correction including chemical shifts and susceptibility by view angle tilting. *Med Phys* 1988;15:7–11.
63. Hargreaves BA, Chen W, Lu W, Alley MT, Gold GE, Brau AC, et al. Accelerated slice encoding for metal artifact correction. *J Magn Reson Imaging* 2010;31:987–96.
64. Li G, Nittka M, Paul D, Lauer L. MSVAT-SPACE for fast metal implants imaging. *Proc Intl Soc Mag Reson Med* 2011;19:3171.
65. Koch KM, Brau AC, Chen W, Gold GE, Hargreaves BA, Koff M, et al. Imaging near metal with a MAVRIC-SEMAC hybrid. *Magn Reson Med* 2011;65:71–82.
66. Rahmer J, Börner P, Dries SP. Assessment of anterior cruciate ligament reconstruction using 3D ultrashort echo-time MR imaging. *J Magn Reson Imaging* 2009;29:443–8.
67. Carl M, Du J, Koch K. Investigations on imaging near metal with combined 3D UTE-MAVRIC. *Proc Intl Soc Mag Reson Med* 2011;19:2668.
68. Seevinck PR, de Leeuw H, Bos C, Bakker CJG. Highly localized positive contrast of small paramagnetic objects using 3D center-out radial sampling with off-resonance reception. *Magn Reson Med* 2011;65:146–56.
69. Koch KM, King KF, Chen W, Gold GE, Hargreaves BA. Frequency encoding in the presence of extreme static field gradients. *Proc Intl Soc Mag Reson Med* 2011;19:293.
70. Monu UD, Worters PW, Sung K, Koch KM, Gold GE, Hargreaves BA. B1 mapping near metallic implants. *Proc Intl Soc Mag Reson Med* 2011;19:3175.
71. Wang K, Yu H, Brittain JH, Reeder SB, Du J. k-space water-fat decomposition with  $T_2^*$  estimation and multi-frequency fat spectrum modeling for ultrashort echo time imaging. *J Magn Reson Imaging* 2010;31:1027–34.
72. Techawiboonwong A, Song HK, Leonard MB, Wehrli FW. Cortical bone water: in vivo quantification with ultrashort echo-time MR imaging. *Radiology* 2008;248:824–33.
73. Anumula S, Wehrli S, Wehrli J, Wright AC, Wehrli FW. Ultra-short echo-time MRI detects changes in bone mineralization and water content in OVX rat bone in response to alendronate treatment. *Bone* 2010;46:1391–9.
74. Du J, Carl M, Bydder M, Takahashi A, Chung CB, Bydder GM. Qualitative and quantitative ultrashort echo time (UTE) imaging of cortical bone. *J Magn Reson* 2010;207:304–11.
75. Rad HS, Lam SC, Magland JF, Ong H, Li C, Song HK, et al. Quantifying cortical bone water in vivo by three-dimensional ultra-short echo-time MRI. *NMR Biomed* 2011;24:855–64.
76. Kokabi N, Bae W, Diaz E, Chung CB, Bydder GM, Du J. Ultrashort TE MR imaging of bovine cortical bone: the effect of water loss on the  $T(1)$  and  $T(2)^*$  relaxation times. *Magn Reson Med* 2011;18:1174–9.
77. Horch RA, Gochberg DF, Nyman JS, Does MD. Selective imaging of bound and pore water in human cortical bone. *Proc Intl Soc Mag Reson Med* 2011;19:1117.
78. Horch RA, Nyman JS, Gochberg DF, Dortch RD, Does MD. Characterization of  $^1\text{H}$  NMR signal in human cortical bone for magnetic resonance imaging. *Magn Reson Med* 2010;64:680–7.
79. Keereman V, Fierens Y, Broux T, De Deene Y, Lonneux M, Vandenberghe S. MRI-based attenuation correction for PET/MRI using ultrashort echo time sequences. *J Nucl Med* 2010;51:812–8.
80. Catana C, van der Kouwe A, Benner T, Michel CJ, Hamm M, Fenchel M, et al. Toward implementing an MRI-based PET attenuation-correction method for neurologic studies on the MR-PET brain prototype. *J Nucl Med* 2010;51:1431–8.
81. Benjamin M, Milz S, Bydder GM. Magnetic resonance imaging of entheses. Part 1. *Clin Radiol* 2008;63:691–703.
82. Benjamin M, Milz S, Bydder GM. Magnetic resonance imaging of entheses. Part 2. *Clin Radiol* 2008;63:704–11.
83. Hodgson RJ, Grainger AJ, O'Connor PJ, Evans R, Coates L, Marzo-Ortega H, et al. Imaging of the Achilles tendon in spondyloarthritis: a comparison of ultrasound and conventional, short and ultrashort echo time MRI with and without intravenous contrast. *Eur Radiol* 2011;21:1144–52.
84. Hauger O, Frank LR, Boutin RD, Lektrakul N, Chung CB, Haghighi P, et al. Characterization of the “red zone” of knee meniscus: MR imaging and histologic correlation. *Radiology* 2000;217:193–200.
85. Gatehouse PD, He T, Puri BK, Thomas RD, Resnick D, Bydder GM. Contrast-enhanced MRI of the menisci of the knee using ultrashort echo time (UTE) pulse sequences: imaging of the red and white zones. *Br J Radiol* 2004;77:641–7.
86. Bydder M, Rahal A, Fullerton GD, Bydder GM. The magic angle effect: a source of artifact, determinant of image

- contrast, and technique for imaging. *J Magn Reson Imaging* 2007;25:290–300.
87. Bydder GM, Chung CB. Magnetic resonance imaging of short  $T_2$  relaxation components in the musculoskeletal system. *Skeletal Radiol* 2009;8:201–5.
  88. Bydder GM. Imaging of short and ultrashort  $T_2$  and  $T_2^*$  tissues using clinical MR systems. *Imaging Med* 2010;2: 225–33.
  89. Wang M, Radjenovic A, Stapleton TW, Venkatesh R, Williams S, Ingham E, et al. A novel and non-destructive method to examine meniscus architecture using 9.4 Tesla MRI. *Osteoarthritis Cartilage* 2010;18:1417–20.
  90. Tsai P-H, Li C, Magland J, Huang T-Y, Wehrli FW, Chung H-W. Demonstration of meniscal fiber structure in vivo by radial imaging with minimal phase excitation and adiabatic fat suppression pulses at high field. *Proc Intl Soc Mag Reson Med* 2011;19:1115.
  91. Du J, Carl M, Diaz E, Takahashi A, Han E, Szeverenyi NM, et al. Ultrashort TE  $T_1\rho$  (UTE  $T_1\rho$ ) imaging of the Achilles tendon and meniscus. *Magn Reson Med* 2010;64:834–42.
  92. Stehling C, Luke A, Stahl R, Baum T, Joseph G, Pan J, et al. Meniscal  $T_1\rho$  and  $T_2$  measured with 3.0T MRI increases directly after running a marathon. *Skeletal Radiol* 2011; 40:725–35.
  93. Williams A, Qian Y, Chu CR. Clinical ultra-short TE-enhanced  $T_2^*$  mapping of meniscus. *Proc Intl Soc Mag Reson Med* 2011;19:562.
  94. Koff MF, Fortier LA, Rodeo SA, Takahashi A, Maher S, Delos D, et al. Temporal and regional changes of  $T_2^*$  in the repaired meniscus. *Proc Intl Soc Mag Reson Med* 2011;19:568.
  95. Gold GE, Thedens DR, Pauly JM, Fechner KP, Bergman G, Beaulieu CF, et al. MR imaging of articular cartilage of the knee: new methods using ultrashort TEs. *AJR Am J Roentgenol* 1998;170:1223–6.
  96. Omoumi P, Teixeira P, Delgado G, Chung CB. Imaging of lower limb cartilage. *Top Magn Reson Imaging* 2009;20: 189–201.
  97. Koff MF, Potter HG. Non-contrast MR techniques and imaging of cartilage. *Radiol Clin North Am* 2009;47: 495–504.
  98. Nissi MJ, Rautiainen J, Lehto LJ, Tiitu V, Kiviranta O, Pulkkinen H, et al. SWIFT imaging of osteochondral repair in equine model with correlation to  $\mu$ CT. *Proc Intl Soc Mag Reson Med* 2011;19:564.
  99. Salo E-N, Nissi MJ, Liimatainen T, Gröhn O, Mangia S, Michaeli S, et al. Multi-parametric MRI assessment of articular cartilage degeneration. *Proc Intl Soc Mag Reson Med* 2011;19:1108.
  100. Law T, Samartzis D, Kim M, Chan Q, Khong P-L, Cheung MK, et al. Ultrashort time-to-echo MRI of the cartilaginous endplate and relationship to degenerative disc disease and Schmorl's nodes. *Proc Intl Soc Mag Reson Med* 2011;19:570.
  101. Moon SM, Yoder JH, Elliott DM, Wehrli FW, Wright AC. In vivo MRI of the cartilaginous endplate of the intervertebral disc. *Proc Intl Soc Mag Reson Med* 2011; 19:1120.
  102. Hall-Craggs MA, Porter J, Gatehouse PD, Bydder GM. Ultrashort echo time (UTE) MRI of the spine in thalassaemia. *Br J Radiol* 2004;77:104–10.
  103. Messiou C, Collins DJ, Robson MD, Bydder GM, Morgan VA, deSouza NM. Quantifying sclerotic bone metastases with 2D ultra short TE MRI: a feasibility study. *Cancer Biomarkers* 2010;7:211–8.
  104. Hiwatashi A, Yoshiura T, Yamashita K, Kamano H, Honda H. Ultrashort TE MRI: usefulness after percutaneous vertebroplasty. *AJR Am J Roentgenol* 2010;195: W365–W368.
  105. Waldman A, Rees JH, Brock CS, Robson MD, Gatehouse PD, Bydder GM. MRI of the brain with ultra-short echo-time pulse sequences. *Neuroradiology* 2003;45:887–92.
  106. Portman O, Flemming S, Cox JP, Johnston DG, Bydder GM. Magnetic resonance imaging of the normal pituitary gland using ultrashort TE (UTE) pulse sequences. *Neuroradiology* 2008;50:213–20.
  107. Lehto LJ, Djaudat I, Corum CA, Garwood M, Gröhn OH. MRI detection of short  $T_2$  component in brain by SWIFT. *Proc Int Soc Mag Reson Med* 2010;17:3326.
  108. Minty EP, Bjarnason TA, Laule C, MacKay AL. Myelin water measurement in the spinal cord. *Magn Reson Med* 2009;61:883–92.
  109. Kolind SH, Mädler B, Fischer S, Li DK, MacKay AL. Myelin water imaging: implementation and development at 3.0T and comparison to 1.5T measurements. *Magn Reson Med* 2009;62:106–15.
  110. Macmillan EL, Mädler B, Fichtner N, Dvorak MF, Li DK, Curt A, et al. Myelin water and  $T(2)$  relaxation measurements in the healthy cervical spinal cord at 3.0T: repeatability and changes with age. *Neuroimage* 2011;54: 1083–90.
  111. Laule C, Vavasour IM, Leung E, Li DK, Kozlowski P, Traboulsee AL, et al. Pathological basis of diffusely abnormal white matter: insights from magnetic resonance imaging and histology. *Mult Scler* 2011;17:144–50.
  112. Horch RA, Gore JC, Does MD. Origins of the ultrashort  $T_2$   $^1\text{H}$  NMR signals in myelinated nerve: a direct measure of myelin content? *Magn Reson Med* 2011;66:24–31.
  113. Wilhelm MJ, Ong HH, Wehrli SL, Tsai P-H, Hackney DB, Wehrli FW. Prospects for quantitative imaging of myelin with dual-echo short inversion time 3D UTE MRI. *Proc Intl Soc Mag Reson Med* 2011;19:2460.
  114. Takahashi M, Togao O, Obara M, van Cauteren M, Ohno Y, Doi S, et al. Ultra-short echo time (UTE) MR imaging of the lung: comparison between normal and emphysematous lungs in mutant mice. *J Magn Reson Imaging* 2010;32:326–33.
  115. Togao O, Tsuji R, Ohno Y, Dimitrov I, Takahashi M. Ultrashort echo time (UTE) MRI of the lung: assessment of tissue density in the lung parenchyma. *Magn Reson Med* 2010;64:1491–8.
  116. Failo R, Wielopolski PA, Tiddens HA, Hop WC, Mucelli RP, Lequin MH. Lung morphology assessment using MRI: a robust ultra-short TR/TE 2D steady state free precession sequence used in cystic fibrosis patients. *Magn Reson Med* 2009;61:299–306.
  117. Corum CA, Idiyatullin D, Moeller S, Chamberlain R, Sachdev D, Garwood M. Lung imaging in the mouse with SWIFT. *Proc Int Soc Mag Res Med* 2010;17:204.
  118. Ohno Y, Koyama H, Yoshikawa T, Aoyama N, Takenaka D, Matsumoto K, et al.  $T_2^*$  measurements of 3.0 T MRI with ultra-short TE: capabilities of pulmonary functional assessment and clinical stage classification in smokers. *Proc Intl Soc Mag Reson Med* 2011;19:3033.
  119. Muradyan I, Hrovat M, Dabaghyan M, Butler J, Hatabu H, Patz S. Pulmonary  $T_2^*$  dependence on the lung volume: preliminary results. *Proc Intl Soc Mag Reson Med* 2011;19:933.
  120. Rajaram S, Swift AJ, Capener D, Condliffe R, Elliot C, Hurdman J, et al. Comparative study of SSPF lung MRI at 1.5T with high resolution computed tomography in patients with interstitial lung fibrosis. *Proc Intl Soc Mag Reson Med* 2011;19:3036.
  121. de Jong S, Zwanenburg JJ, Visser F, van der Nagel R, van Rijen HV, Vos MA, et al. Direct detection of postinfarction myocardial fibrosis with ultrashort TE (UTE) MRI. *Proc Intl Soc Mag Reson Med* 2011;19:1352.
  122. Chappell KE, Patel N, Gatehouse PD, Main J, Puri BK, Taylor-Robinson SD, et al. Magnetic resonance imaging of

- the liver with ultrashort TE (UTE) pulse sequences. *J Magn Reson Imaging* 2003;18:709–13.
123. Wansapura JP, Daniel BL, Vigen KK, Butts K. In vivo MR thermometry of frozen tissue using  $R2^*$  and signal intensity. *Acad Radiol* 2005;12:1080–4.
  124. Kaye EA, Josan S, Lu A, Rosenberg J, Daniel BL, Pauly KB. Consistency of signal intensity and  $T_2^*$  in frozen ex vivo heart muscle, kidney, and liver tissue. *J Magn Reson Imaging* 2010;31:719–24.
  125. Chan CF, Keenan NG, Nielles-Vallespin S, Gatehouse P, Sheppard MN, Boyle JJ, et al. Ultra-short echo time cardiovascular magnetic resonance of atherosclerotic carotid plaque. *J Cardiovasc Magn Reson* 2010;12:17.
  126. Sharma S, Boujraf S, Bornstedt A, Hombach V, Ignatius A, Oberhuber A, et al. Quantification of calcification in endarterectomy samples by means of high-resolution ultra-short echo time imaging. *Invest Radiol* 2010;45:109–13.
  127. Du J, Corbeil J, Znamirovski R, Angle N, Peterson M, Bydder GM, et al. Direct imaging and quantification of carotid plaque calcification. *Magn Reson Med* 2010;65:1013–20.
  128. Robson MD, Gatehouse PD, So PW, Bell JD, Bydder GM. Contrast enhancement of short  $T_2$  tissues using ultrashort TE (UTE) pulse sequences. *Clin Radiol* 2004;59:720–6.
  129. Tymofiyeva O, Boldt J, Rottner K, Schmid F, Richter EJ, Jakob PM. High-resolution 3D magnetic resonance imaging and quantification of carious lesions and dental pulp in vivo. *MAGMA* 2009;22:365–374.
  130. Djaudat I, Corum CA, Moeller S, Prasad HS, Garwood M, Nixdorf DR. SWIFT versus X-ray in dental imaging. *Proc Int Soc Mag Reson Med* 2010;17:543.
  131. Bracher AK, Hofmann C, Bornstedt A, Boujraf S, Hell E, Ulrici J, et al. Feasibility of ultra-short echo time (UTE) magnetic resonance imaging for identification of carious lesions. *Magn Reson Med* 2011;66:538–45.
  132. Rühli FJ, von Waldburg H, Nielles-Vallespin S, Böni T, Speier P. Clinical magnetic resonance imaging of ancient dry human mummies without rehydration. *JAMA* 2007;298:2618–20.
  133. Ra, JB, Hilal SK, Cho ZH. A method for in vivo MR imaging of the short  $T_2$  component of sodium-23. *Magn Reson Med* 1986;3:296–302.
  134. Nielles-Vallespin S, Weber MA, Bock M, Bongers A, Speier P, Combs SE, et al. 3D radial projection technique with ultrashort echo times sodium MRI: clinical applications in human brain and skeletal muscle. *Magn Reson Med* 2007;57:74–81.
  135. Atkinson IC, Sonstegaard R, Pliskin NH, Thulborn KR. Vital signs and cognitive function are not affected by 23-sodium and 17-oxygen magnetic resonance imaging of the human brain at 9.4T. *J Magn Reson Imaging* 2010;32:82–7.
  136. Lu A, Atkinson IC, Claiborne TC, Damen FC, Thulborn KR. Quantitative sodium imaging with a flexible twisted projection pulse sequence. *Magn Reson Med* 2010;63:1583–93.
  137. Atkinson IC, Thornton KR. Feasibility of mapping the tissue mass corrected bioscale of cerebral metabolic rate of oxygen consumption using 17-oxygen and 23-sodium MR imaging in a human brain at 9.4 T. *Neuroimage* 2010;51:723–33.
  138. Lu A, Atkinson IC, Thulborn KR. In vivo brain sodium  $T_2^*$  mapping with a multiple-echo flexible TPI sequence. *Proc Intl Soc Mag Reson Med* 2011;19:3504.
  139. Ouwerkerk R, Bottomley PA, Solaiyappan M, Spooner AE, Tomaselli GF, Wu KC, et al. Tissue sodium concentration in myocardial infarction in humans: a quantitative  $^{23}\text{Na}$  MR imaging study. *Radiology* 2008;248:88–96.
  140. Furlan A, Moon C-H, Kim J-H, He X, Park B, Zaho T, et al. Sodium MR imaging of human kidney using a dual-tuned ( $^{23}\text{Na}/^1\text{H}$ ) body RF coil at 3T: quantitative assessment of sodium concentration and corticomedullary gradient in healthy subjects. *Proc Intl Soc Mag Reson Med* 2011;19:2947.
  141. Kalayciyan R, Wetterling F, Neudecker S, Schad LR. In vivo, sodium imaging of kidney using 3D ultrashort echo time sequence. *Proc Intl Soc Mag Reson Med* 2011;19:1489.
  142. Madelin G, Lee JS, Inati S, Jerschow A, Regatte RR. Sodium inversion recovery MRI of the knee joint in vivo at 7T. *J Magn Reson* 2010;207:42–52.
  143. Wang L, Wu Y, Chang G, Oesingmann N, Schweitzer ME, Jerschow A, et al. Rapid isotropic 3D-sodium MRI of the knee joint in vivo at 7T. *J Magn Reson Imaging* 2009;30:606–14.
  144. Chang G, Wang L, Schweitzer ME, Regatte RR. 3D  $^{23}\text{Na}$  MRI of human skeletal muscle at 7 Tesla: initial experience. *Eur Radiol* 2010;20:2039–46.
  145. Robson MD, Tyler DJ, Neubauer S. Ultrashort TE chemical shift imaging (UTE-CSI). *Magn Reson Med* 2005;53:267–74.
  146. Ackerman JL, Wu Y, Reese TG, Cao H, Hrovat ML, Toddes SP, et al. In vivo  $^{31}\text{P}$  solid state MRI of human wrists: short- $T_2$  MRI using the scanner  $^1\text{H}$  channel. *Proc Intl Soc Mag Reson Med* 2011;19:427.
  147. Hitchens TK, Ye Q, Ho C. 3D ultra short TE MRI for whole subject imaging of perfluorocarbon-labeled cell biodistribution. *Proc Intl Soc Mag Reson Med* 2011;19:1706.
  148. Qian Y, Williams AA, Chu CR, Boada FE. Multicomponent  $T_2^*$  mapping of knee cartilage: technical feasibility ex vivo. *Magn Reson Med* 2010;64:1426–31.
  149. Williams A, Qian Y, Bear D, Chu CR. Assessing degeneration of human articular cartilage with ultrashort echo time (UTE)  $T_2^*$  mapping. *Osteoarthritis Cartilage* 2010;18:539–46.
  150. Williams A, Qian Y, Chu CR. UTE-  $T_2^*$  mapping of human articular cartilage in vivo: a repeatability assessment. *Osteoarthritis Cartilage* 2011;19:84–8.
  151. Filho GH, Du J, Pak BC, Statum S, Znamorowski R, Haghighi P, et al. Quantitative characterization of the Achilles tendon in cadaveric specimens:  $T_1$  and  $T_2^*$  measurements using ultrashort-TE MRI at 3 T. *AJR Am J Roentgenol* 2009;192:W117–24.
  152. Kirsch S, Schad LR. Single-slice mapping of ultrashort  $T(2)$ . *J Magn Reson* 2011;210:133–6.
  153. Du J, Pak BC, Znamirovski R, Statum S, Takahashi A, Chung CB, et al. Magic angle effect in magnetic resonance imaging of the Achilles tendon and enthesis. *Magn Reson Imaging* 2009;27:557–64.
  154. Szeverenyi NM, Bydder GM. Dipolar anisotropy fibre imaging in a goat knee meniscus. *Magn Reson Med* 2011;65:463–70.
  155. Atkinson IC, Lu A, Thulborn KR. Characterization and correction of system delays and eddy currents for MR imaging with ultrashort echo-time and time-varying gradients. *Magn Reson Med* 2009;62:532–7.
  156. Josan S, Pauly JM, Daniel BL, Pauly KB. Double half RF pulses for reduced sensitivity to eddy currents in UTE imaging. *Magn Reson Med* 2009;61:1083–9.
  157. Josan S, Kaye E, Pauly JM, Daniel BL, Pauly KB. Improved half RF slice selectivity in the presence of eddy currents with out-of-slice saturation. *Magn Reson Med* 2009;61:1090–5.
  158. Takizawa M, Hanada H, Oka K, Takahashi T. Correcting K-trajectory by using multiple function models of gradient waveform for ultrashort TE (UTE). *Proc Intl Soc Mag Reson Med* 2011;19:4385.

159. Madio DP, Lowe IJ. Ultra-fast imaging using low flip angles and FIDs. *Magn Reson Med* 1995;34:525–9.
160. Hsu J-J, Lowe IJ. Signal recovery in free induction decay imaging using a stimulated spin echo. *Magn Reson Med* 2002;47:409–14.
161. Paley MNJ, Kryukov E, Lamperth M, Young IR. An independent multichannel imaging research system for ultrashort echo time imaging on clinical MR systems. *Concepts Mag Reson Part B: Mag Reson Eng* 2009;35B:80–8.
162. Hafner S. Fast imaging in liquids and solids with the Back-projection Low Angle ShoT (BLAST) technique. *Magn Reson Imaging* 1994;12:1047–51.
163. Grodzki DM, Jakob PM, Heismann B. Ultra short echo time imaging using pointwise encoding time reduction with radial acquisition (PETRA). *Proc Intl Soc Mag Reson Med* 2011;19:2815.
164. Weiger M, Stampanoni M, Pruessmann KP. Direct depiction of bone microstructure using ZTE imaging. *Proc Intl Soc Mag Reson Med* 2011;19:563.
165. Gurney PT, Hargreaves BA, Nishimura DG. Design and analysis of a practical 3D cones trajectory. *Magn Reson Med* 2006;55:575–82.
166. Du J, Bydder M, Takahashi AM, Chung CB. Two-dimensional ultrashort echo time imaging using a spiral trajectory. *Magn Reson Imaging* 2008;26:304–12.
167. Hetzer S, Mildner T, Möller HE. A modified EPI sequence for high-resolution imaging at ultra-short echo time. *Magn Reson Med* 2011;65:165–75.
168. Krämer P, Konstandin S, Heilmann M, Schad LR. 3D radial twisted projection imaging for DCE-MRI with variable flip angles. *Proc Intl Soc Mag Reson Med* 2011;19:2055.
169. Martirosian P, Schraml C, Schwenzler NF, Springer F, Schick F, Deimling M. Magnetic resonance imaging of tendons, ligaments and menisci by subtraction of two steady free precession signals. *Proc Intl Soc Mag Reson Med* 2011;19:2724.
170. Diwoy C, Stollberger R. 3D radial bUTE. *Proc Intl Soc Mag Reson Med* 2011;19:387.
171. Kijowski R, Klaers J, Lee K, Rosas H, Hernandez L, Block W. Rapid multi-planar assessment of the articular cartilage of the knee joint using isotropic resolution VIPR-ATR imaging. *Proc Intl Soc Mag Reson Med* 2011;19:503.
172. Petersen W, Tillmann B. Collagenous fibril texture of the human knee joint menisci. *Anat Embryol* 1998;197:317–24.
173. Bogduk N. The inter-body joint and the intervertebral discs. In: *Clinical anatomy of the lumbar spine and sacrum*. 3rd edn. Churchill Livingstone: Edinburgh, UK: 1997;13.